J. Fluid Mech. (1993), *vol.* 254, *pp.* 229–250

Finite-amplitude instability of mixed convection

By **B. B. ROGERS, S. GHOSH MOULIC** AND **L. S. YAO**

Department of Mechanical and Aerospace Engineering, Arizona State University, Tempe,
AZ 85287, USA

(Received 15 May 1992 and in revised form 3 March 1993)

The finite-amplitude instability of mixed convection of air in a vertical concentric annulus with each cylinder maintained at a different temperature is studied by use of weakly nonlinear instability theory and by direct numerical simulation. A strictly shear instability and two thermally induced instabilities exist in the parameter space of Reynolds and Grashof numbers. The first thermal instability occurs at low Reynolds numbers as the rate of heating increases, and is called a thermal-shear instability because it is a shear-driven instability induced by thermal effects. The second thermal instability occurs at larger Reynolds number as heating increases, and is also a thermally induced shear instability called the interactive instability. The weakly nonlinear results demonstrate that the thermal-shear instability is supercritical at all wavenumbers. With the shear and interactive instabilities, however, both subcritical and supercritical branches appear on the neutral curves. The validity of the weakly nonlinear calculations are verified by comparison with a direct simulation. The results for subcritical instabilities show that the weakly nonlinear calculations are accurate when the magnitude of the amplification rate is small, but the accuracy deteriorates for large amplification rates. However, the trends predicted by the weakly nonlinear theory agree with those predicted by the direct simulations for a large portion of the parameter space. Analyses of the energy sources for the disturbance show that subcritical instability of the shear and interactive modes occurs at larger wavenumbers because of increased gradient production of disturbance kinetic energy. This is because, at shorter wavelengths, the growth of the wave causes the shape of the fundamental disturbance to change from that predicted by linear instability theory to a shape more favourable for shear-energy production. The results also show that many possibly unstable modes may be present simultaneously. Consequently, all of these modes, as well as all of the possible wave interactions among the modes, must be considered to obtain a complete picture of mixed-convection instability.

1. Introduction

Mixed convection occurs in many engineering systems, as well as in the atmosphere. Mixed convection differs from isothermal flow due to the buoyancy effects induced by heating. Only in the limit of zero heating is the flow isothermal. Different heating conditions result in distinctive temperature distributions and, consequently, different flow fields and instability characteristics. Experimental results in circular pipes indicate that these flows become unstable at relatively low heating rates and Reynolds numbers (Scheele & Hanratty 1962; Kemeny & Somers 1962; Maitra & Subba Raju 1975), and a steady, parallel non-isothermal flow has rarely been observed. In spite of these results, in the analysis of non-isothermal flow inside ducts the flow has often been incorrectly treated as a parallel flow, and many correlations for heat transfer coefficients and friction factors have been developed based on these oversimplified models. In this paper, we will provide insight into this complex problem by studying the finite-amplitude instability of mixed convection in a vertical concentric annulus with each wall maintained at a different temperature using weakly nonlinear instability theory, as well as a direct numerical simulation.

In practical systems, the thermal boundary conditions frequently can be approximated as a linear combination of two conditions: the temperature and the heat flux. The conditions of constant temperature and constant heat flux can be accurately and easily set up in the laboratory. However, the basic states are different for each case, and linear instability analyses of mixed convection in vertical annuli have demonstrated that the instability characteristics differ substantially. In case I, each cylinder was maintained at a different temperature (Yao & Rogers 1989*a*, *b*). In case II, a constant heat flux was imposed on the inner cylinder, and the outer cylinder was insulated (Rogers & Yao 1992*a*).

For case I, the results for air (Prandtl number $Pr = 0.71$) demonstrated that the instability boundary consists of three distinct instabilities, identified by their characteristic wavenumbers and wave speeds. The *shear* instability occurs at large Reynolds numbers. The critical Reynolds number for the shear instability in mixed-convection flows is, however, different from that of isothermal flow. This is because the difference in temperature between the walls induces a thermal stratification, and the resulting buoyant forces modify the velocity profiles. In addition, at fixed Reynolds number, Re, thermal instability can occur when the temperature difference between the walls increases, such that the corresponding ratio of Grashof and Reynolds numbers (Gr/Re) reaches its critical value. This thermal instability approaches natural-convection instability as Re decreases to zero. As Re increases, the critical (Gr/Re) initially decreases, but soon becomes almost independent of Re. Analysis of the energy transfer in mixed convection has shown that there are two sources of kinetic energy to sustain the instability. The first of these is the shear production, which is the product of the Reynolds stress and the mean-flow strain rate, and the second is the buoyant potential. The low-Re thermal instability originates with an unstable velocity distribution caused by buoyant forces, but most of the kinetic energy for this instability is obtained by shear production. Therefore, this is a shear instability induced by thermal effects, and is called the *thermal-shear* instability. As Gr/Re and Re increase, another thermal instability appears that bridges the gap between the thermal-shear and the shear instabilities. This instability also obtains energy primarily through shear production, and is called the *interactive* instability.

The linear stability results of case II demonstrated that, in addition to the shear and thermal-shear instabilities, two more thermally induced instabilities may appear. When the vertical temperature gradient is negative, a *Rayleigh–Taylor* type instability is possible since the vertical density stratification is unstable. However, in the stably stratified case, the Rayleigh–Taylor mode is not present, and a thermal instability occurs as the Rayleigh number, which characterizes the magnitude of the vertical-temperature gradient in this case, increases. This instability will be of thermal-shear type at small Prandtl numbers, but at large Prandtl numbers, the instability obtains kinetic energy primarily by buoyant production. This is called the *thermal-buoyant* instability. The minimum critical value of the Rayleigh number was found to be a very weak function of Re for Re greater than 200, and the shape of the instability boundary in the (Ra, Re)-plane is similar for both the thermal-shear and thermal-buoyant instabilities. However, the least stable value of the Rayleigh number is much smaller for the thermal-buoyant instability at large Pr than it is for the thermal-shear mode at small *Pr*. Experimental heat-transfer results are available for the flow of water in the stably stratified flow for case II (Maitra & Subba Raju 1975), and the heat-transfer results predicted by weakly nonlinear instability theory (Yao & Rogers 1992 herein referred to as YR) agreed very well with the data.

The linear stability results for case I have demonstrated that the physics differs from that of case II, including the appearance of the interactive instability and of non-axisymmetric modes. In this paper, we study the finite-amplitude instability of this problem and compare the results with those of a direct numerical simulation. The details of the weakly nonlinear theory are given in YR, and are not repeated here.

An advantage of weakly nonlinear instability theory is that the required computational effort is modest, yet it provides accurate results when the magnitude of the amplification rate is small. However, the range of validity of the theory has not been established with certainty using perturbation methods. For plane-Poiseuille flow, Sen & Venkateswarlu (1983) included many terms in the perturbation series and investigated its convergence. Their results demonstrated that the Landau–Stuart series converges rapidly only when the magnitude of the amplification rate is small. As the magnitude of the amplification rate increases, the series converges more slowly, and soon begins to diverge. These results did not, however, establish the range for which the perturbation method produces accurate results. In this paper, we include only one additional term in the series, and compare the amplitude predicted by both perturbation theories to the results of a direct numerical simulation at selected points. Our results show that if the predictions of the lowest-order theory agree with the higher-order theory, they will also agree with the direct simulation. Therefore, when the results from both perturbation theories are in agreement, the predictions are reliable, and verification by a direct simulation is unnecessary in these cases.

In §2, the problem of mixed convection in a vertical annulus with each wall maintained at a different temperature is formulated. The results of the weakly nonlinear analysis in §3 show that the thermal-shear instability is supercritical. On the other hand, both the shear and interactive instabilities may be subcritical or supercritical at the least-stable wavenumbers. However, the modes are always subcritical at other nearby wavenumbers. The comparison of the techniques for determining the subcritical threshold velocity shows that when the amplification, characterized by the imaginary portion of the eigenvalue c_i is small, the results are in agreement. As $|c_i|$ increases, the results begin to diverge. On one hand, the results of the direct simulation demonstrate that, even though the threshold amplitudes are inaccurate, the trends predicted by the weakly nonlinear calculations are correct for a substantial range of $|c_i|$. The calculations show, on the other hand, that the weakly nonlinear results are not accurate in the subcritical region for $|c_i| > 0.01$. The results of the calculations in the supercritical region demonstrate that the weakly nonlinear method can be extended further than is the case for subcritical instability. Analysis of the energy sources for the disturbance demonstrates that subcritical instability occurs at larger wavenumbers primarily because of increased gradient production of disturbance kinetic energy. This is because the shape of the fundamental disturbance changes from that predicted by linear instability theory to a shape more favourable for shear energy production at shorter wavelengths. The results also indicate that for both subcritical and supercritical instabilities, many possibly unstable modes may be present at the same values of *Gr*/*Re* and *Re*. Consequently, all of these modes, as well as all of the possible wave interactions among the modes, must be considered to obtain a complete picture of mixed-convection instability.

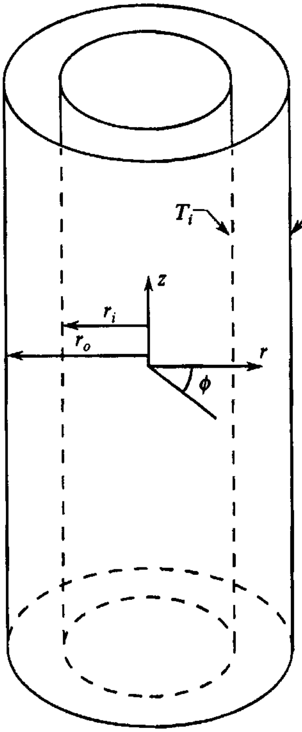

FIGURE 1. Geometry and coordinates.

2. Analysis

2.1. *Formulation*

In this paper, pressure-driven non-isothermal flow in a vertical concentric annulus, as illustrated in figure 1, is considered. The temperatures of the inner and outer cylinders are T_i and T_o, respectively. The governing equations are the Boussinesq equations in cylindrical coordinates:

$$\frac{\partial u}{\partial \eta}+\frac{u}{\eta+K}+\frac{1}{\eta+K}\frac{\partial v}{\partial \phi}+\frac{\partial w}{\partial z}=0, \tag{1a}$$

$$\frac{\partial u}{\partial t}+u\frac{\partial u}{\partial \eta}+\frac{v}{\eta+K}\frac{\partial u}{\partial \phi}+w\frac{\partial u}{\partial z}-\frac{v^2}{\eta+K}=-\frac{\partial P}{\partial \eta}+\frac{1}{Re}\left[\mathrm{D}^2 u-\frac{1}{(\eta+K)^2}\left\{2\frac{\partial v}{\partial \phi}+u\right\}\right], \tag{1b}$$

$$\frac{\partial v}{\partial t}+u\frac{\partial v}{\partial \eta}+\frac{v}{\eta+K}\frac{\partial v}{\partial \phi}+w\frac{\partial v}{\partial z}+\frac{uv}{\eta+K}=-\frac{1}{\eta+K}\frac{\partial P}{\partial \phi}+\frac{1}{Re}\left[\mathrm{D}^2 v+\frac{1}{(\eta+K)^2}\left\{2\frac{\partial u}{\partial \phi}-v\right\}\right], \tag{1c}$$

$$\frac{\partial w}{\partial t}+u\frac{\partial w}{\partial \eta}+\frac{v}{\eta+K}\frac{\partial w}{\partial \phi}+w\frac{\partial w}{\partial z}=-\frac{\partial P}{\partial z}+\frac{1}{Re}[\mathrm{D}^2 w]+\frac{Gr}{Re^2}\theta, \tag{1d}$$

$$\frac{\partial \theta}{\partial t}+u\frac{\partial \theta}{\partial \eta}+\frac{v}{\eta+K}\frac{\partial \theta}{\partial \phi}+w\frac{\partial \theta}{\partial z}=\frac{1}{Re\,Pr}[\mathrm{D}^2\theta], \tag{1e}$$

where

$$\mathrm{D}^2=\frac{\partial^2}{\partial \eta^2}+\frac{1}{\eta+K}\frac{\partial}{\partial \nu}+\frac{1}{(\eta+K)^2}\frac{\partial^2}{\partial \phi^2}+\frac{\partial^2}{\partial z^2}.$$

The z-coordinate has been made dimensionless by scaling with the gap width, r_o-r_i.

The dimensionless radial coordinate is $\eta = (r-r_i)/(r_o-r_i)$ and the curvature parameter is $K = r_i/(r_o-r_i)$. The dimensionless temperature is given by $\theta = (T-T_o)/(T_i-T_o)$. The velocities are scaled by the mean axial velocity, W_{ave}, the pressure by $\rho(W_{ave})^2$, and time by $(r_o-r_i)/W_{ave}$. The parameters in the problem are the Reynolds number, $Re = W_{ave}(r_o-r_i)/\nu$, the Prandtl number, $Pr = \nu/\gamma$, and the Grashof number, $Gr = \beta g(r_o-r_i)^3(T_i-T_o)/\nu^2$, where g is the gravitational acceleration, β the thermal expansion coefficient, ν the kinematic viscosity and γ the thermal diffusivity. The boundary conditions for the velocity components are the no-slip and no-penetration conditions on the concentric cylinders. The temperature boundary conditions are $\theta(0) = 1$ and $\theta(1) = 0$.

2.2. *Basic state and linear instability*

The basic state is a fully developed, laminar parallel flow and a corresponding temperature distribution (Yao & Rogers 1989*a*). The equations for the basic state are given by

$$\frac{\mathrm{d}^2 W_0}{\mathrm{d}\eta^2} + \frac{1}{\eta+K}\frac{\mathrm{d}W_0}{\mathrm{d}\eta} + \frac{Gr}{Re}\Theta_0 = Re\frac{\mathrm{d}P_0}{\mathrm{d}z}, \tag{2a}$$

$$\frac{\mathrm{d}^2\Theta_0}{\mathrm{d}\eta^2} + \frac{1}{\eta+K}\frac{\mathrm{d}\Theta_0}{\mathrm{d}\eta} = 0. \tag{2b}$$

The product of the axial pressure gradient and the Reynolds number may be determined by the requirement of global mass conservation:

$$\int_0^1 W(\eta+K)\,\mathrm{d}\eta = \tfrac{1}{2}(1+2K). \tag{2c}$$

Therefore, the basic-state velocity and temperature profiles depend only on the curvature parameter, K, and the ratio Gr/Re. The solution of (2) is described in Yao & Rogers (1989*a*). The results show that as Gr/Re increases, the fluid near the warmer wall is accelerated by buoyant forces, leading to a corresponding deceleration of the fluid near the colder wall so that mass is conserved. The velocity profiles are thus distorted by buoyancy, leading to the appearance of inflexion point, which indicates a potential for instability.

To determine the linear stability of the basic state, the dependent variables are split into a basic state and a small disturbance, as follows:

$$u(\eta,\phi,z,t) = \hat{u}(\eta)\,\mathrm{e}^{\mathrm{i}\alpha(z-ct)+\mathrm{i}n\phi}, \tag{3a}$$

$$v(\eta,\phi,z,t) = \hat{v}(\eta)\,\mathrm{e}^{\mathrm{i}\alpha(z-ct)+\mathrm{i}n\phi}, \tag{3b}$$

$$w(\eta,\phi,z,t) = W_0(\eta) + \hat{w}(\eta)\,\mathrm{e}^{\mathrm{i}\alpha(z-ct)+\mathrm{i}n\phi}, \tag{3c}$$

$$\theta(\eta,\phi,z,t) = \Theta_0(\eta) + \hat{\theta}C(\eta)\,\mathrm{e}^{\mathrm{i}\alpha(z-ct)+\mathrm{i}n\phi}, \tag{3d}$$

where W_0 and Θ_0 are the basic-state velocity and temperature distributions respectively, and the $\hat{}$ denotes a small-disturbance quantity. The standard normal-mode form has been assumed for the disturbance, where α is the axial wavenumber, and n is the integer azimuthal wavenumber. The expressions given by (3) are substituted into the governing equations, the basic state is subtracted, and the small nonlinear terms are neglected. This results in a set of ordinary differential equations which describe the small disturbance. These equations form a linear eigenvalue problem for the complex disturbance wave speed, c, with the disturbance being unstable for $c_i > 0$ and stable for $c_i < 0$.

2.3. *Weakly nonlinear instability analysis*

To study the finite-amplitude instability of the basic state using weakly nonlinear theory, the dependent variables are first separated into Fourier components of a disturbance wave predicted by linear-instability theory. The equations governing the harmonic components are then solved using a perturbation expansion. In YR, the first correction to the exponential growth predicted by linear-instability theory was obtained, and the results were compared to experimental data. In the present case, there are no experimental results available for comparison. Therefore, we investigate the accuracy of the perturbation method more carefully by including one more term in the expansion. The Fourier expansion of, for example, the axial velocity is

$$w(\eta,\phi,z,t) = W(\eta,\tau_1,\tau_2)\,E^0 + w_1(\eta,\tau_1,\tau_2)\,E^1 + w_2(\eta,\tau_1,\tau_2)\,E^2 + w_3(\eta,\tau_1,\tau_2)\,E^3 + \dots + \text{c.c.}, \tag{4}$$

where $E = \exp(\mathrm{i}\alpha(z-c_r t)+\mathrm{i}n\phi)$, and c.c. stands for complex-conjugate. The inclusion of E^4 and higher harmonics is not necessary in the present analysis. The disturbance wave speed c_r is obtained from linear-instability theory at the particular values of Gr/Re, Re, α, and n under consideration. Substituting this expansion, as well as similar expansions for the other dependent variables, into the governing equations and separating out Fourier components results in sets of equations for each wave component.

The functions for each harmonic component are further expanded in terms of the small parameter c_i. In this paper, the procedure used in YR is followed, and terms up to order $(c_i)^{\frac{5}{2}}$ are considered. Using the method of multiple timescales, with $(t, \tau_1 = c_i t,\ \tau_2 = c_i^2 t)$, results in

$$\frac{\partial}{\partial t} = \frac{\partial}{\partial t} + c_i\frac{\partial}{\partial \tau_1} + c_i^2\frac{\partial}{\partial \tau_2}. \tag{5}$$

The consistent expansion of the E^1 wave is

$$\hat{w}_1(\eta,\tau_1,\tau_2) = c_i^{\frac{1}{2}} B_1(\tau_1,\tau_2)\,w_{10}(\eta) + c_i^{\frac{3}{2}}[B_1|B_1|^2\,w_{11} + B_2(\tau_1,\tau_2)\,w_{10}] + c_i^{\frac{5}{2}}\,\bar{w}_{12}(\eta,\tau_1,\tau_2) + O(c_i^{\frac{7}{2}}), \tag{6}$$

where $B_1(\tau_1,\tau_2)$ and $B_2(\tau_1,\tau_2)$ are order-one amplitude functions. Expansions for the other components of the E^1 wave are given by similar expressions. The expansion for the E^1 wave given by (6) leads to specific algebraic expressions for the expansions of the forced waves, E^0, E^2 and E^3. The result is a system of equations which may be solved sequentially in increasing powers of c_i. The expansion represents a small modification to that of Stuart (1960), in that the terms involving the difference between the basic-state velocity and the complex disturbance wave speed, $W_0 - c$, are considered to be order one. This is because the finite-amplitude disturbance is expressed as a perturbation on the state of a finite amplification rate, c_i. At third order $(O(c_i)^{\frac{3}{2}})$, the E^1 equations become non-homogeneous equations with the left-hand sides consisting of the linear-instability operators operating on the functions u_{11}, v_{11}, w_{11} and θ_{11}, and the right-hand sides consisting of terms proportional to $\partial B_1/\partial\tau_1$, B_1 and $B_1|B_1|^2$. The coefficients of the terms on the right-hand sides consist of functions determined from the analysis of the E^0 and E^2 waves at second order. Since the homogeneous forms of the equations in this case are those of the linear-instability problem, the integrability condition requires that the non-homogeneous terms be orthogonal to the functions satisfying the homogeneous adjoint problem. This leads to the following amplitude equation for B_1:

$$\partial B_1/\partial \tau_1 = \alpha B_1 + a_1 B_1|B_1|^2. \tag{7}$$

The constant a_1 is called the first Landau constant, and is obtained through the application of the integrability condition. This equation differs from the ordinary differential equation obtained in YR due to the inclusion of the additional slow timescale τ_2. If higher-order terms are not considered, (7) predicts supercritical instability if the real part of a_1 is negative, with an equilibrium amplitude of $|A_1|^2 = c_i|B_1|^2 = -\alpha c_i/(a_i)$, where $(\,)_r$ denotes the real part. If $(a_1)_r$ is positive, a subcritical instability is predicted with $|A_1|^2 = |\alpha c_i/(a_1)_r|$. (In this paper, the eigenvectors have been normalized so that the numerical value of $|A|^2$ represents the ratio of the disturbance kinetic energy to that of the mean flow.)

To obtain a more accurate result, terms up to fifth-order $(O(c_i)^{\frac{5}{2}})$ are considered. At this order, the E^1 equations again become non-homogeneous with the homogeneous parts consisting of the linear-instability operators operating on the functions $\bar{u}_{12}$, $\bar{v}_{12}$, w_{12}, and $\bar{\theta}_{12}$. The non-homogeneous terms are proportional to $\partial B_1/\partial \tau_2$, $\partial B_2/\partial \tau_1$, B_2, $B_1|B_1|^2$, $B_1|B_1|^4$, $B_2|B_1|^2$, and $\tilde{B}_2(B_1)^2$. The integrability condition at this order leads to the following amplitude equation:

$$\frac{\partial B_1}{\partial \tau_2} + \frac{\partial B_2}{\partial \tau_1} = \alpha B_2 + \lambda_1 B_1|B_1|^2 + \lambda_2 B_2|B_1|^2 + \lambda_3 \tilde{B}_2 B_1^2 + a_2 B_1|B_1|^4. \tag{8}$$

The coefficients of the amplitude function in this equation are also determined through application of the integrability condition. Following the procedure described by Fujimura (1989), it is possible to show that $a_1 = \frac{1}{2}\lambda_2 = \lambda_3$. Making use of these relations, adding (7) and (8), and keeping terms up to order c_i, the following single amplitude equation is obtain:

$$\partial B/\partial \tau = \alpha B + (a_1 + c_i \lambda_1) B|B|^2 + c_i a_2 B|B|^4, \tag{9}$$

where $B = B_1 + c_i B_2$ and $\partial/\partial \tau = \partial/\partial \tau_1 + c_i \partial/\partial \tau_2$. Therefore, the amplitude predicted by this equation represents an order-c_i correction to the amplitude predicted by the Landau equation at order $(c_i)^{\frac{3}{2}}$.

It is worth pointing out that all of the coefficients in (9) are determined uniquely by the integrability conditions, with no additional constraints on the system, as would be necessary in an amplitude-expansion theory. Furthermore, the problem of mean-flow resonance in the subcritical region (Davey & Nguyen 1971) does not occur in this method. These points have been discussed in detail in YR.

2.4. *Direct numerical simulation*

The Navier–Stokes system was solved numerically as an initial value problem using a spectral collocation method in space and finite differences in time. The spatial discretization is based on Fourier expansions in the axial and azimuthal directions and Chebyshev polynomials in the radial direction. The dependent variables are represented by expansions of the form

$$u(\eta, \phi, z, t) = \sum_{n=-\frac{1}{2}N_z}^{\frac{1}{2}N_z-1} \sum_{m=-\frac{1}{2}N_\phi}^{\frac{1}{2}N_\phi-1} \hat{u}(\eta, m, n, t)\, \mathrm{e}^{\mathrm{i}[m\phi + n\alpha(z - c_r t)]}, \tag{10a}$$

$$\hat{u}(\eta, m, n, t) = \sum_{k=0}^{N_y} \tilde{u}(k, m, n, t)\, T_k(y), \tag{10b}$$

where α is the fundamental wavenumber in the axial direction, c_r is the phase speed of the waves predicted by linear-instability theory, $T_k(y)$ is the kth degree Chebyshev polynomial defined by $T_k(y) = \cos(k \cos^{-1} y)$, $y = 2\eta - 1$, and N_y, N_z and N_ϕ are the number of collocation points in the radial, axial and azimuthal directions, respectively. The collocation points are

$$y_j = \cos\left(\frac{\pi j}{N_y}\right), j = 0, 1, \ldots, N_y, \quad z_j = \frac{2\pi}{\alpha N_z}, j = 0, 1, \ldots, N_z - 1,$$

$$\phi_j = \frac{2\pi j}{N_\phi}, j = 0, 1, \ldots, N_\phi - 1. \tag{11}$$

This choice of collocation points yields 'spectral accuracy' and allows fast transformation of variables between physical space and wave space. Time differencing was done using a Crank–Nicolson scheme for the diffusion terms, backward Euler for the pressure and second-order Adams–Bashforth for the convection and body force terms. The rotation form of the Navier–Stokes equations is preferred for the numerical simulations because, as noted by Orszag (1972), the use of this form guarantees that Fourier collocation methods conserve kinetic energy and ensures that the nonlinear terms do not cause numerical instability. Time-differencing errors are reduced by using a coordinate system moving with the constant phase speed of the wave, as indicated by (10*a*), although, because of Galilean invariance, this is equivalent to a calculation in a frame of reference which is at rest. The momentum equations are decoupled by solving a Poisson equation for the pressure. The correct boundary conditions for the pressure, consistent with a divergence-free velocity field at the solid boundaries, are obtained by an influence matrix technique (Kleiser & Schumann 1980, 1984). The numerical procedure is essentially the same as that of Kleiser & Schumann, which requires the solution of a sequence of Helmholtz equations at each time step. These equations are solved by a preconditioned minimum residual method (Canuto *et al.* 1988).

3. Results

3.1. *Review of linear-instability results*

The linear-instability boundary in the $(Gr/Re, Re)$ plane for mixed convection of air in an annulus was determined in Yao & Rogers (1989*a*), and is shown on figure 2. In this earlier paper, it was demonstrated that at $K = 10$, the least-stable infinitesimal disturbances are often non-axisymmetric, and the effects of curvature are clearly present. Consequently, since the linear instability results are well known and the important physical effects of curvature are present in this case, this geometry was chosen for the present study as well.

The definition of Gr used in this paper gives the result that when Gr/Re is positive, the inner cylinder is at a higher temperature than the outer cylinder. As figure 2 illustrates, the shape of the linear-instability boundary depends on whether the inner or outer cylinder is warmer, except at values of Re below 100, where the results are symmetric about the $Gr/Re = 0$ axis. At small values of Re, the flow becomes linearly unstable to thermally induced instability as the magnitude of Gr/Re increases. This instability is determined to be a *thermal-shear* instability, since it obtains most of its kinetic energy from shear production. For positive Gr/Re, the azimuthal wavenumbers of the least-stable thermal-shear instability varies from $n = 19$ at $Re = 6000$ to $n = 0$ at Re below 500, and the least-stable linear disturbances may be non-axisymmetric in

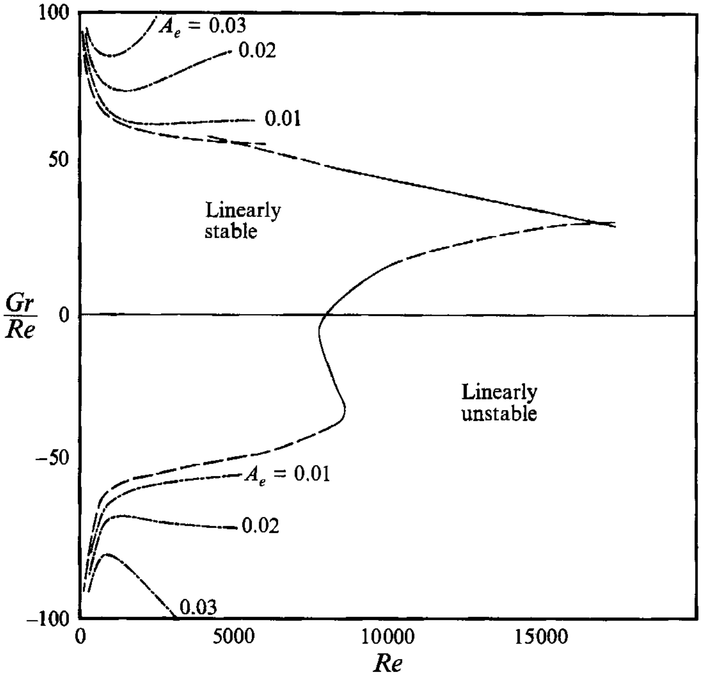

FIGURE 2. Stability diagram in $(Gr/Re, Re)$-coordinates.

this case. At negative values of Gr/Re, on the other hand, the least-stable thermal-shear disturbances are axisymmetric at all values of Re.

In isothermal flow $(Gr/Re = 0)$, the motion becomes linearly unstable to an axisymmetric shear instability at $Re = 7876$, as illustrated. For positive Gr/Re, this instability is stabilized as Gr/Re increases. For negative Gr/Re, this instability is initially destabilized by decreasing Gr/Re, but as Gr/Re decreases further, the instability is stabilized, although not as sharply as it is for $Gr/Re > 0$. In all cases, the least-stable azimuthal mode is axisymmetric for the shear instability.

In between the thermal-shear and the shear instabilities is the interactive instability. For Gr/Re greater than zero, the interactive instability forms a distinct curve, and may be identified from the shear and thermal-shear instability curves by characteristic wavenumbers and wave speeds, even in the regions where the curves intersect. The least-stable azimuthal wavenumber varies in this case from $n = 13$ at $Re = 5000$ to $n = 0$ for $Re = 8000$ and larger. For Gr/Re less than zero, on the other hand, the linear-instability boundary also consists of thermal-shear, interactive and shear instabilities, but the curves blend together smoothly, and no distinguishing characteristics, such as wavenumber or wave speed, can be used to separate the instabilities. The range of each instability has been identified in this case by considering the evolution, with increasing Re, of the wavenumbers and wave speeds, and the thermally induced instability was determined to be the thermal-shear mode for $Re < 2000$, and the interactive mode for $Re > 2000$.

3.2. *Weakly nonlinear results near the neutral curves*

Since the lowest-order weakly nonlinear analysis is asymptotically correct in the limit as c_i approaches zero, the theory may be used to predict the behaviour of the linear modes at the least-stable values of Gr/Re and Re. In figure 2, the neutral-stability boundaries are made up of two types of lines, solid and broken. The solid lines indicate

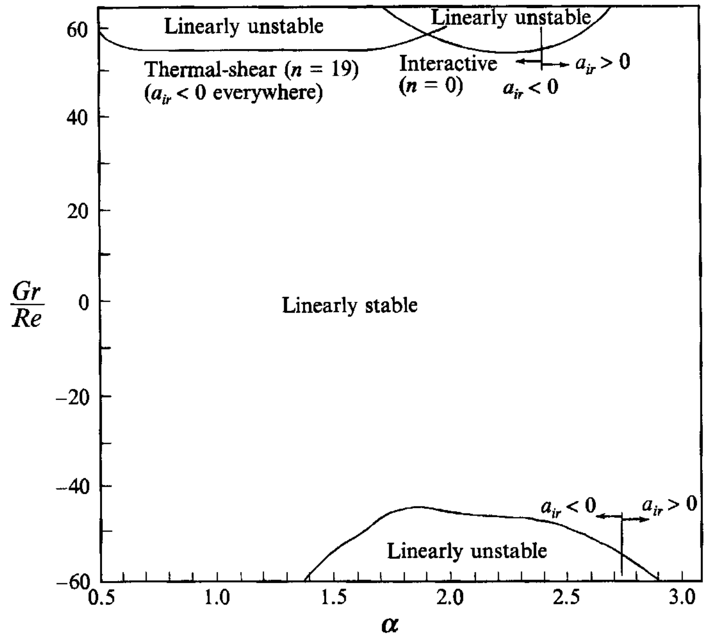

FIGURE 3. Linear stability diagram in $(Gr/Re, \alpha)$-coordinates for $Re = 6000$.

subcritical instability $((a_1)_r > 0)$ while the broken lines indicate supercritical instability $((a_1)_r < 0)$ at the least-stable wavenumbers for linear instability. In this problem, we find that the thermal-shear instability is supercritical at all wavenumbers, while, on their respective neutral curves, the shear and interactive instabilities are subcritical at larger axial wavenumbers, and supercritical at smaller wavenumbers. This is illustrated on figures 3 and 4, which are plots of the neutral curves in the $(Gr/Re, \alpha)$-plane at $Re = 6000$ and 13000, respectively. On figure 3, the axisymmetric interactive modes for positive and negative values of Gr/Re are shown, along with the non-axisymmetric $(n = 19)$ thermal-shear mode. As mentioned, for the thermal-shear instability, the value of $(a_1)_r$ is negative at all wavenumbers, and this is a supercritical instability. Also, it is seen that the variation of the least-stable value of Gr/Re with the axial wavenumber is small for this instability. This is also true of the azimuthal wavenumber (Yao & Rogers 1989*a*). Consequently, this instability has a large band of supercritically unstable wavenumbers, which will begin to grow at nearly the same value of Gr/Re.

The minimum critical value of Gr/Re for the axisymmetric interactive mode shown on figure 3 is slightly larger than that for the non-axisymmetric interactive mode (55.3 as opposed to 55.2). On the other hand, with the non-axisymmetric interactive mode, the value of $(a_1)_r$ is negative at all values of the axial wavenumber. However, with $n = 0$, $(a_1)_r$ becomes positive for $\alpha > 2.43$, and subcritical instabilities will exist at these wavenumbers. At negative Gr/Re, the flow first becomes linearly unstable to an axisymmetric disturbance at $Gr/Re = -46$. The instability is supercritical for a band of wavenumbers around the least-stable wavenumber, but at wavenumbers greater than 2.75, $(a_1)_r$ changes sign, and subcritical instability occurs.

The neutral curves for the shear and interactive instabilities at $Re = 13000$ shown on figure 4 illustrate that the value of $(a_1)_r$ for the shear instability is negative at the least-stable wavenumber, but becomes positive as α increases, and subcritical shear instabilities will exist at larger wavenumbers. With the interactive instability at this Re, the value of $(a_1)_r$ is positive for α greater than 2.05, and subcritical instability will exist

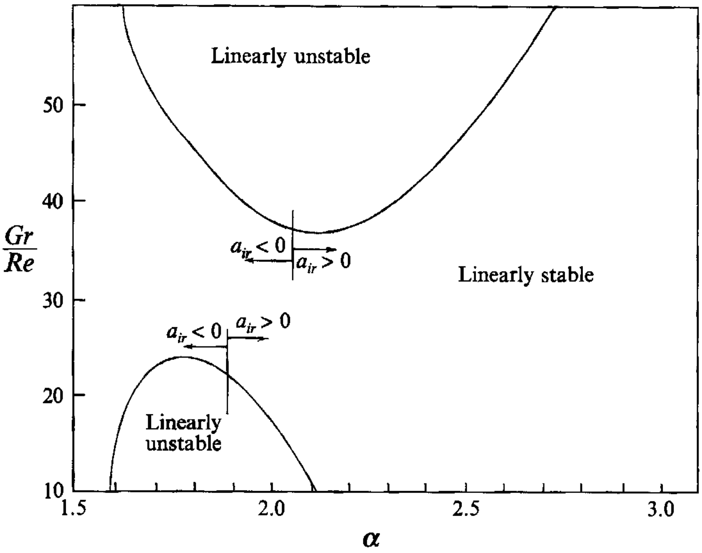

FIGURE 4. Linear stability diagram in $(Gr/Re, \alpha)$-coordinates for $Re = 13000$.

at these wavenumbers. Comparison with figure 3 illustrates that with the interactive instability, the wavenumber above which subcritical instability exists decreases as *Re* increases. This is reflected on figure 2, which shows that at $Re = 8200$, the interactive instability boundary changes from a dashed line, indicating supercritical instability at the least-stable wavenumbers, to a solid line, indicating subcritical instability at these points. On the other hand, with shear instability, as *Re* increases, the least-stable wavenumbers become supercritical. However, at all *Re*, subcritical instability exists with the shear instability at larger axial wavenumbers.

These results also demonstrate that more than one type of instability may be present at the same values of Gr/Re and *Re*. For example, figure 3 illustrates that at $Gr/Re = 60$ at $Re = 6000$, both the thermal-shear and interactive instabilities are present. Furthermore, the thermal-shear instability is unstable to a large waveband of disturbances between $\alpha = 0.5$ and $\alpha = 2$. The interactive instability is also supercritically unstable in a waveband between $\alpha = 1.85$ and $\alpha = 2.6$. At $\alpha > 2.6$, the axisymmetric interactive instability is linearly stable, but subcritical instability exists at these wavenumbers. Furthermore, with the thermal-shear instability at smaller wavenumbers, the results on figure 3 demonstrate that the free oscillations of the harmonic wave will exist at slightly supercritical values of Gr/Re since the E^2 wave also becomes linearly unstable. All of these possibilities must be considered in a complete simulation of mixed-convection instability. To study these phenomena requires development of a wave-interaction theory for a continuous spectrum of unstable waves, which we are presently undertaking.

3.3. *Comparison of weakly nonlinear results with direct simulations*

In the subcritical region, the minimum value of the threshold amplitude for instability A_t at a particular combination of Gr/Re and *Re*, is determined by a search of the (α, n)-space. It has been determined that the value of the minimum threshold amplitude varies substantially with the axial wavenumber α. However, in all cases investigated, the least-stable azimuthal wavenumber for subcritical finite-amplitude instability is $n = 0$.

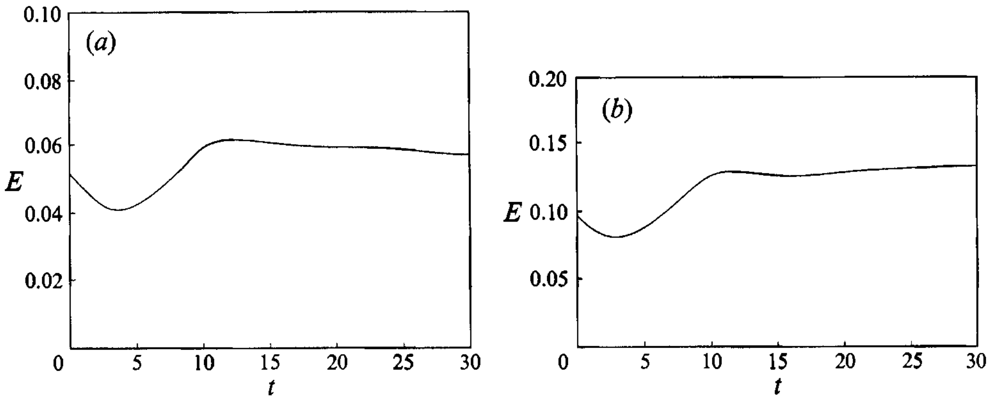

FIGURE 5. Time history of the disturbance kinetic energy obtained from the direct simulations at $Gr/Re = 30$, $Re = 6000$, $\alpha = 3.0$ for two different initial amplitudes.

In addition to the linearly unstable modes, additional linearly stable modes were investigated which are potentially subcritically unstable. In this study, the ten least-stable linear modes have all been analysed. The lowest-order weakly nonlinear theory predicts that, in addition to the shear and interactive modes, there is a subcritically unstable thermal-buoyant mode. However, in all cases, the higher-order weakly nonlinear theory predicts opposite results for the same mode. Furthermore, the threshold amplitudes predicted by the lowest-order theory are very large for this disturbance, so that the temperature fluctuations necessary to trigger the instability are of the same order as the basic state. Therefore, this mode is not considered in this paper.

To determine the range of validity of weakly nonlinear results, they are compared with results of a direct numerical simulation of the Navier–Stokes equations at selected points in the parameter space $(Gr/Re, Re)$. The threshold amplitude for subcritical instability for given values of Gr/Re, Re and α was determined from the direct numerical simulations by making several runs with different initial amplitudes. The initial conditions used for the computations are of the form:

$$\begin{aligned} u &= A\hat{u}(\eta)\,\mathrm{e}^{\mathrm{i}\alpha z} + \text{c.c.}, \\ v &= A\hat{v}(\eta)\,\mathrm{e}^{\mathrm{i}\alpha z} + \text{c.c.}, \\ w &= W_0(\eta) + A\hat{w}(\eta)\,\mathrm{e}^{\mathrm{i}\alpha z} + \text{c.c.}, \\ \theta &= \Theta_0(\eta) + A\hat{\theta}(\eta)\,\mathrm{e}^{\mathrm{i}\alpha z} + \text{c.c.}, \end{aligned}$$

where W_0 and Θ_0 are the basic-state velocity and temperature profiles, respectively, A is the disturbance amplitude, $\hat{u}$, $\hat{v}$, $\hat{w}$ and $\hat{\theta}$ are the linear-instability eigenfunctions and c.c. denotes the complex-conjugate. The solution was marched forward in time until the initial transients decayed and a steady growth or decay rate could be determined. The threshold amplitude was then determined by linear interpolation of these results. To illustrate the interpolation process used to determine the threshold amplitudes, we consider a specific case in which the parameters are $Gr/Re = 30$, $Re = 6000$, $\alpha = 3$. The time history of the disturbance kinetic energy, E, for this case is shown in figures 5(*a*) and 5(*b*) for two different initial amplitudes. Figure 5(*a*) indicates a steady decay of the disturbance after an initial transient period, while figure 5(*b*) indicate a steady growth rate. The steady growth or decay rate $\mathrm{d}E/\mathrm{d}t$ is plotted in figure 6 as a function of the initial disturbance kinetic energy E_0 for four values of E_0. Figure 6 indicates that the

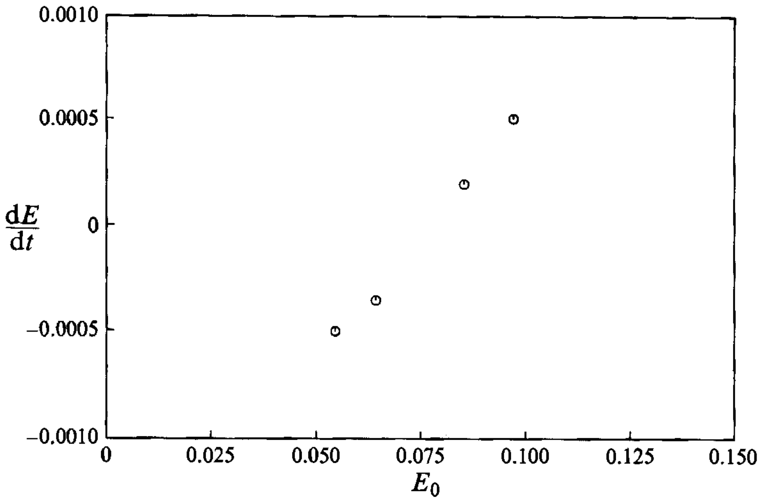

FIGURE 6. The growth rate of the disturbance kinetic energy obtained from the direct simulations at $Gr/Re = 30$, $Re = 6000$, $\alpha = 3.0$ as a function of the initial disturbance kinetic energy.

	Subcritical model	Supercritical mode
Gr/Re	30	120
Re	6000	150
α	3.0	2.5
A	0.1217×10^{-5}	0.6935×10^{-3}
C_r	0.51675	0.83414
Computed c_r	0.51525	0.83417
c_i	−0.03414	0.06974
Computed c_i	−0.03467	0.06968

TABLE 1. Behaviour of small-amplitude disturbances; time step $\Delta t = 0.05$, final time $T = 10$

relation between dE/dt and E_0 is linear for small values of dE/dt. Thus, linear interpolation may be used to obtain the threshold value of the initial disturbance kinetic energy, E_t, for which $dE/dt = 0$.

The computations were done on the CRAY-XMP supercomputer at Arizona State University using 33 Chebyshev polynomials in the radial direction, 32 Fourier modes in the axial direction, 8 Fourier modes in the azimuthal direction and a time step $\Delta t = 0.005$. The accuracy of the numerical method was tested by comparing the numerically determined growth rates and wave speeds with linear theory. The results of two such tests are summarized in table 1, which shows that the growth rates and phase speeds computed from the direct simulations for small-amplitude disturbances are in good agreement with those predicted by linear theory. Adequate spatial resolution was ensured by monitoring the energies in the highest Fourier modes. As noted by Marcus (1981), severe truncation in the number of Fourier modes results in an artificial curl in the high-wavenumber end of the energy spectrum. Our spectra did not exhibit such a curl. The energy in the largest axial wavenumber mode was found to be so small that aliasing errors are negligible compared to the time-stepping errors. The energy in the azimuthal Fourier modes ($m \neq 0$) was found to be zero for the cases considered in this investigation, that is, the flow remained axisymmetric.

Typical results of the calculation of the threshold amplitudes for subcritical

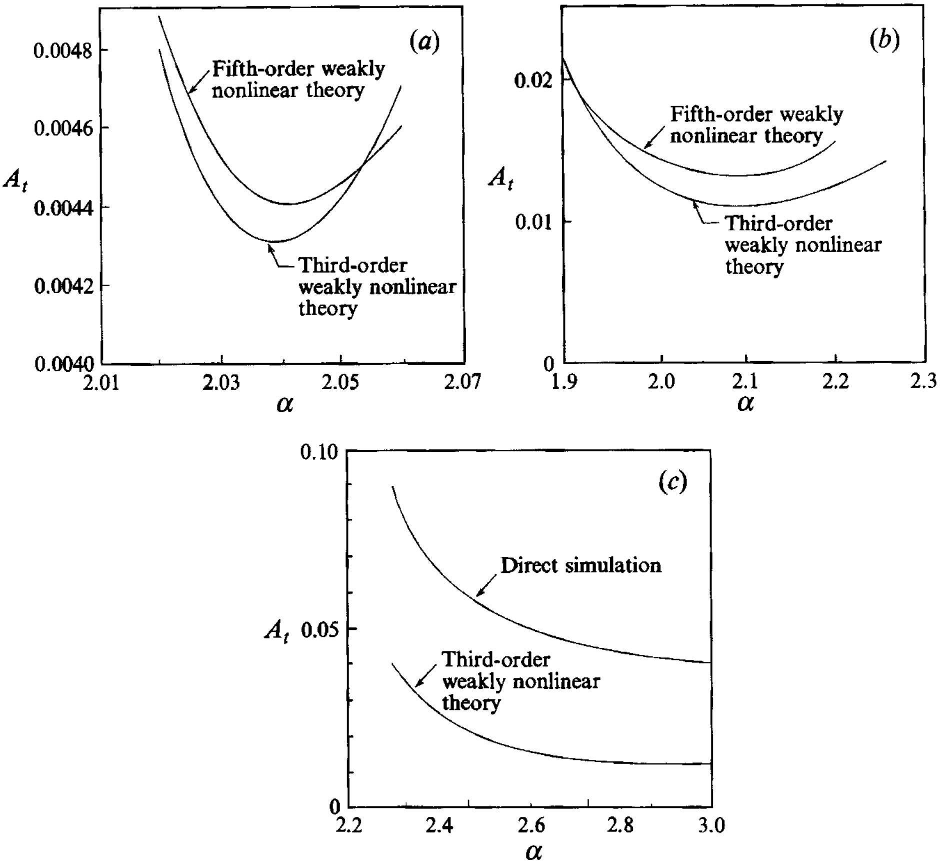

FIGURE 7. Threshold amplitude *vs.* axial wavenumber in the subcritical region. (*a*) $Re = 7876$ and $Gr/Re = 3$. (*b*) $Re = 7876$ and $Gr/Re = 10$. (*c*) $Re = 6000$ and $Gr/Re = 30$.

instabilities are illustrated on figure 7. Figure 7(*a*) is a plot of A_t *vs.* α as predicted by both weakly nonlinear theories for the axisymmetric shear mode at $Re = 7876$ and $Gr/Re = 3$, near the critical point of isothermal flow, which is $Re = 7876$, $Gr/Re = 0$. The minimum threshold amplitudes predicted by each theory agree within 2% at this condition. Figure 7(*b*) is a plot of A_t *vs.* α at $Re = 7876$ and $Gr/Re = 10$. In this case, the fifth-order theory predicts a value which is 15% larger than that predicted by the third-order theory. Figure 7(*b*) also illustrates that the wavenumber of the most unstable finite-amplitude disturbance is increasing with respect to the least-stable linear mode as $|c_i|$ increases. This is further shown by figure 7(*c*), which is a plot of A_t *vs.* α at $Re = 6000$ and $Gr/Re = 30$. In this case, a distinct minimum in the A_t *vs.* α curve does not exist, but rather the minimum value of A_t approaches 0.012 as α increases. At this point, the fifth-order theory does not predict a threshold amplitude. Similar results are observed throughout the $(Gr/Re, Re)$-plane when the magnitude of the amplification rate increase, and the fifth-order theory does not provide a check on the accuracy of the third-order theory in these cases. Therefore, the validity of this analysis has been investigated by comparing the third-order results to those predicted by the direct simulation. Figure 7(*c*) shows that the direct simulation predicts a larger threshold amplitude at all wavenumbers. However, the trend predicted by the direct simulation is the same as that predicted by the weakly nonlinear theory: the threshold amplitude for subcritical instability decreases with increasing wavenumbers.

Re	*Gr/Re*	A_t (third-order)	A_t (fifth-order)	A_t (direct)
4000	0	0.0185	—	—
4000	10	0.017	—	—
4000	30	0.0156	—	—
6000	0	0.0146	—	0.024
6000	10	0.0125	—	0.041
6000	30	0.0122	—	0.043
7876	3	0.0043	0.0044	0.0041
7876	10	0.016	0.013	0.025
7876	30	0.0103	—	0.026
9000	30	0.0096	—	0.023
11000	30	0.0086	—	0.019
13000	30	0.008	—	0.01
15000	30	0.0063	—	0.007

TABLE 2. Subcritical threshold amplitudes in the $(Gr/Re, Re)$-plane calculated by the third-order weakly nonlinear method, the fifth-order weakly nonlinear method and by the direct simulation; — denotes that the method failed to predict a threshold amplitude for instability at the given condition

The values of the minimum subcritical threshold amplitudes predicted by the weakly nonlinear theories and the direct simulation are given in table 2 for a range of values of Gr/Re and Re. The third-order theory predicts a subcritical threshold amplitude at values of Re above 2000 for all Gr/Re. However, the results are unreliable in this region because the perturbation technique may not be extended this far. To determine the range for which the results are reliable, we compare the threshold amplitudes for instability predicted by the three techniques as c_i increases. At $Re = 7876$ and $Gr/Re = 3$, the value of c_i is -0.00021, and the amplitudes predicted by the third-order theory, the fifth-order theory and the direct simulation are in agreement. At $Re = 7876$ and $Gr/Re = 10$, the value of c_i is -0.00188. Here, the amplitude predicted by the third-order theory and the fifth-order theory differ more substantially, and the direct simulation predicts a value of A_t which is 2.2 times as large as that predicted by the third-order theory. Therefore, all theories still predict a subcritical threshold amplitude at this point, but the numerical values of A_t do not agree as well as they did when the magnitude of c_i was smaller. At $Re = 6000$ and $Gr/Re = 10$, $c_i = 0.04$, and the fifth-order theory does not predict a threshold amplitude at this point, while the direct simulation predicts an amplitude 3.3 times as large as that predicted by the third-order theory. Therefore, subcritical instability exists at this point as predicted by the third-order theory, but the threshold amplitude for instability predicted by the theory is inaccurate. At $Re = 4000$, and $Gr/Re = 10$, $c_i = -0.05$, and the third-order theory predicts $A_t = 0.017$. However, as with the fifth-order theory, in this case the direct simulation also fails to predict a threshold amplitude. Clearly, neither the results nor the trends predicted by the weakly nonlinear theory are reliable at this point. The results discussed here illustrate that when both the third- and fifth-order calculations predict threshold amplitudes, the direct simulation will also predict a threshold amplitude. Therefore, in this problem, the predictions are reliable when both the third- and fifth-order theories produce similar results, and verification by a direct simulation is unnecessary in these cases. However, the results of the third-order theory are not necessarily invalid after the fifth-order method has broken down. To fully determine the range of applicability of the third-order results, they must be compared with those obtained by the direct simulation.

As the data in table 2 indicate, the numerical agreement between the weakly nonlinear results and those of the direct simulation improves as Re increases. For example, at $Re = 6000$ and $Gr/Re = 30$, the threshold amplitude predicted by the direct simulation is 3.5 times as large as that predicted by the third-order theory. At $Re = 7876$ and $Gr/Re = 30$, the ratio decreases to 2.5. This ratio continues to decrease as Re increases, and at $Re = 15000$ and $Gr/Re = 30$, the direct method predicts a threshold amplitude that is only 10% larger than that of the weakly nonlinear theory. It is worth pointing out that at $Gr/Re = 30$, in all cases the fifth-order theory has failed to predict a threshold amplitude. This is because the minimum threshold amplitude in these cases occurs at an axial wavenumber of $\alpha = 3$, as was illustrated in figure 7(*c*). Therefore, even though the value of Gr/Re was close to the minimum critical value, since the wavenumber is substantially different than the critical wavenumber, the magnitude of c_i is too large for the fifth-order method to converge.

With the thermal-shear instability, at small Re, the subcritical shear and interactive instabilities do not appear, and finite-amplitude equilibrium states will exist for the thermal-shear disturbances when the magnitude of Gr/Re exceeds the minimum critical value. These regions are shown on figure 2, where the contours of constant supercritical equilibrium amplitude are plotted for this instability at both positive and negative values of Gr/Re. At Re less than 1000 the critical value of Gr/Re is increasingly rapidly. As a result, at fixed Gr/Re in this region, the equilibrium amplitude will increase as Re increases. However, at Re greater than 1000, $(Gr/Re)_c$ approaches a constant value, and the amplitude begins to decrease with increasing Re. These results also illustrate that both the linear-instability boundary and the contours of constant equilibrium amplitude are close to symmetric about the $Gr/Re = 0$ axis at small Re.

At $Gr/Re = 120$ and $Re = 150$, the value of c_i is 0.07. The equilibrium amplitude predicted by the third-order theory at this point is $A_e = 0.0694$, that predicted by the fifth-order theory is $A_e = 0.0692$, and the direct simulation predicts $A_e = 0.085$. Therefore, the agreement between the third- and fifth-order results is very good, and the direct simulation is in reasonable agreement with the weakly nonlinear results. The agreement is much better in this case than it was in the subcritical region, where the results began to diverge when the magnitude of c_i was less than 0.01. This is consistent with the results of Sen & Venkateswarlu (1983), who studied a supercritical portion of the neutral curve for plane-Poiseuille flow, and also found that the weakly nonlinear theory was valid for a larger range in the supercritical region than it was in the subcritical region. This also explains why the heat-transfer rates in the annulus with a vertical temperature gradient imposed on the inner cylinder that were predicted by the third-order finite-amplitude theory or a supercritical instability in YR compared well with the experimental data of Maitra & Subba Raju (1975) over a wide range of heating rates.

In the subcritical region, the lack of prediction of a threshold amplitude by the higher-order theory as c_i increases is similar to the behaviour observed in plane-Poiseuille flow by Sen & Venkateswarlu (1983), who used the equilibrium-amplitude method. They found that, except when the magnitude of the amplification rate was small, if the series sum was truncated at even orders, no threshold amplitude was predicted, in contrast to the results when the series was truncated at odd order. By considering the first 19 Landau coefficients and using Shank's method to extend their results, they determined the 'true sum' of the series. They found that at $(Re-Re_c)/Re_c = 0.13$, the result predicted by the lowest-order theory was 25% smaller than that predicted by the true sum of the series. These results lead to the conclusion that in this problem, at $Re = 6000$ and $Gr/Re = 10$, the inclusion of more terms in the expansion is unlikely to bring the amplitudes predicted by the weakly nonlinear method into agreement with the direct simulation, and the perturbation technique has reached its limit at this point. This demonstrates that the range for which the weakly nonlinear theory may be used to accurately predict the threshold amplitude for instability is limited in this case. However, the results have also demonstrated that the trends predicted by the weakly nonlinear theory agree with those of the direct simulation for a larger range. Consequently, the theory may be used to complete a parametric study of the instabilities in complex flows, such as this, where the cost of a complete study by a direct simulation is prohibitive. The weakly nonlinear results may then be used to identify a few conditions to be studied in detail by a numerical simulation.

3.4. *Energy transfer*

The appearance of subcritical instability at larger wavenumbers in the shear and interactive instabilities leads us to study the nature of the instability in more detail by considering the energy transfer in the non-isothermal flow. As is discussed in YR, in non-isothermal flows, the potential energy of density waves and the kinetic energy of momentum waves is transferable. Therefore, the disturbance waves may gain kinetic energy from both shear production, which is the product of the Reynolds stresses and the mean-flow strain-rate, and buoyant production, caused by the fluctuating body force. The transfer of thermal energy to the momentum wave occurs because components of the disturbance heat flux exist both in the balance of disturbance kinetic energy and in the balance of thermal variance. In vertically stratified flows, as was the case in YR, the exchange occurs directly at the same wavelength along the direction of the body force. In non-stratified flows, as is the case in this paper, there are no mean gradients in the direction of the body force, and the equations for the balance of thermal variance and disturbance kinetic energy are not directly coupled. In this case, the transfer of energy occurs indirectly between the radial disturbance heat flux, $\overline{u\theta}$, which appears in the gradient production term in the balance of thermal variance, and the axial disturbance heat flux, $\overline{w\theta}$, which appears in the buoyant production term in the balance of disturbance kinetic energy. These heat flux components interact with each other because the axial and radial disturbance velocities are coupled through pressure scrambling (Rogers & Yao 1992*b*).

As explained by Stuart (1960), the balance of kinetic energy for the fundamental disturbance leads the amplitude equation:

$$\frac{\mathrm{d}|B|^2}{\mathrm{d}\tau} = 2\alpha|B|^2+(\mathscr{P}_{101}+\mathscr{E}_{12}+\mathscr{P}_{110}+\mathscr{T}_{11}+\mathscr{D}_{11})\,|B|^4. \tag{12}$$

The expressions for the balance of kinetic energy for the fundamental wave as well as the terms in (12) are given in the Appendix. Comparison of (12) with (7) shows that

$$2a_{1r} = \mathscr{P}_{101}+\mathscr{E}_{12}+\mathscr{P}_{110}+\mathscr{T}_{11}+\mathscr{D}_{11}. \tag{13}$$

The physical interpretation of the terms in (13) is as follows. The first term, $\mathscr{P}_{101}$, represents the gradient production of kinetic energy due to the interaction between the fundamental disturbance and the distorted mean velocity gradient. Since the energy required for the distortion of the mean flow is obtained from the fundamental disturbance, this term will always be negative. Consequently, if only this term is considered (Stuart 1958) a supercritical disturbance will always be predicted. The second term, $\mathscr{E}_{12}$, represents the flow of energy from the fundamental wave due to the harmonic. The last three terms, $\mathscr{P}_{110}$, $\mathscr{T}_{11}$ and $\mathscr{D}_{11}$ all represent energy exchange due to

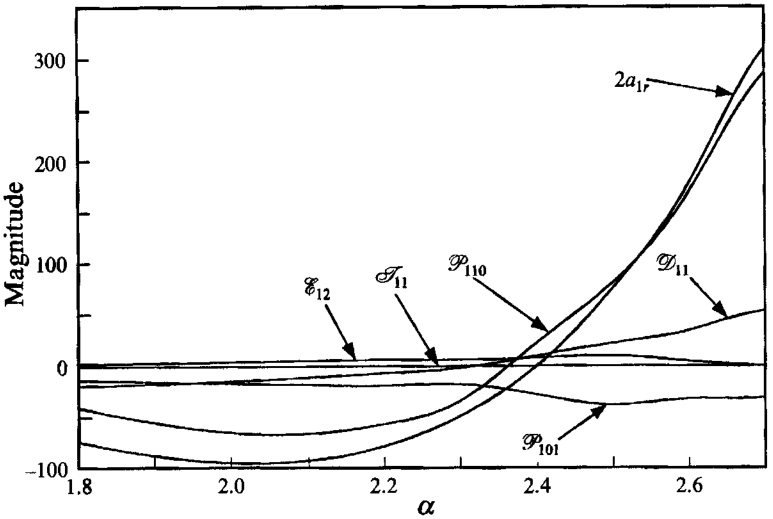

FIGURE 8. Plot of terms in (13) *vs.* the axial wavenumber for the interactive instability at $Re = 6000$ and $Gr/Re = 50$.

the modification of the shape of the fundamental disturbance. The term $\mathscr{P}_{110}$ represents the modification in the gradient production of disturbance energy due to the change of the disturbance shape. It is important to note that this term, in contrast to $\mathscr{P}_{101}$, may be either positive or negative. If the term is positive, the change in the shape of the disturbance enhances the gradient production of disturbance energy. The term $\mathscr{T}_{11}$ represents the change in the buoyant production of disturbance energy due to the change in shape of the fundamental wave. The last term, $\mathscr{D}_{11}$, represents a modification in the viscous dissipation of disturbance kinetic energy due to the change in the disturbance shape. Therefore, this term also may be of either sign. If $\mathscr{D}_{11}$ is positive, the change of shape of the fundamental wave results in a decrease in the rate of dissipation of the disturbance.

By investigating the magnitude of the terms in (13), the important physical processes that lead to a change from supercritical ($a_{1r} < 0$) to subcritical ($a_{1r} > 0$) instability with increasing wavenumber for the shear and interactive instabilities may be enumerated. This is illustrated on figure 8, which is a plot of the terms in (13) *vs.* the axial wavenumber for the interactive instability at $Re = 6000$ and $Gr/Re = 50$. In this case, a_{1r} becomes positive for $\alpha > 2.4$. As discussed above, these results demonstrate that the value of $\mathscr{P}_{101}$ is negative at all wavenumbers, and this effect will always tend to stabilize a subcritical flow. The terms $\mathscr{T}_{11}$ and $\mathscr{C}_{12}$ are very small, and account for less than 3% of the Landau constant. On the other hand, the terms that account for modification in the gradient production and viscous dissipation due to the disturbance growth, $\mathscr{P}_{110}$ and $\mathscr{D}_{11}$, are more significant. It is these terms, along with $\mathscr{P}_{101}$, that represent the important physical processes that lead to subcritical instability. As the results show, the variation of $\mathscr{P}_{101}$ with wavenumber is relatively small. The plot of $\mathscr{D}_{11}$ demonstrates that the change in shape of the disturbance increases the rate of dissipation at wavenumbers below $\alpha = 2.32$, and decreases it at larger wavenumbers. Therefore, this effect becomes destabilizing to subcritical flows at wavenumbers greater than $\alpha = 2.32$. However, the dominant effect in this case is the modification of the shear production of disturbance energy due to the change in shape of the disturbance, as the plot of $\mathscr{P}_{110}$ demonstrates. This effect is stabilizing below $\alpha = 2.34$, but becomes destabilizing thereafter. As the

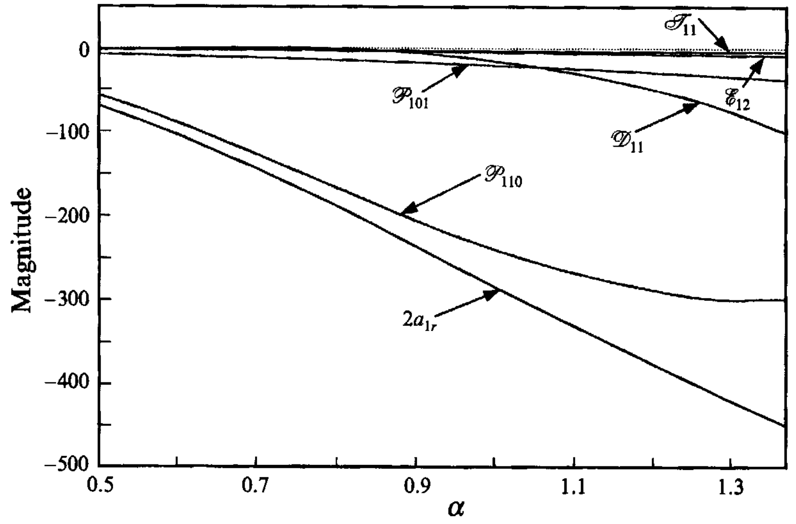

FIGURE 9. Plot of terms in (13) *vs.* the axial wavenumber for the thermal-shear instability at $Re = 6000$ and $Gr/Re = 60$.

plot of a_{1r} on figure 8 demonstrates, the value of the Landau constant becomes positive above $\alpha = 2.4$, when the combined destabilizing effects of $\mathscr{P}_{110}$ and $\mathscr{D}_{11}$ overcome the stabilizing effect of $\mathscr{P}_{101}$. As the wavenumber increases further, $\mathscr{P}_{110}$ increases rapidly, thus increasing the magnitude of the Landau constant and tending to decrease the magnitude of the threshold amplitude for subcritical instability. These results demonstrate that the subcritical instability of the interactive mode at large wavenumbers is primarily due to enhanced shear production of disturbance energy at these conditions. This occurs because, at the larger wavenumbers, the shape of the fundamental disturbance is modified due to the (nonlinear) finite-amplitude effects from that of the infinitesimal disturbance predicted by linear theory to a shape more favourable for shear energy production.

To investigate the energy transfer in the supercritical thermal-shear instability, the terms in (13) have bee plotted *vs.* the axial wavenumber at $Re = 6000$ and $Gr/Re = 60$ on figure 9. These results illustrate that all of the nonlinear terms are stabilizing in the sense that an increase in the disturbance amplitude results in a decrease in the rate of growth of the disturbance. However, in this case, the disturbance is already linearly unstable. Consequently, the nonlinear effects limit the growth of the disturbance, resulting in a finite-amplitude equilibrium state. Similar to the subcritical interactive instability, the transfer of energy to the harmonic and the modification of buoyant energy production, quantified by $\mathscr{E}_{12}$ and $\mathscr{T}_{11}$ respectively, are small compared to the other terms. The transfer of energy from the disturbance back to the mean flow, given by $\mathscr{P}_{101}$, decreases nearly linearly with increasing wavenumber, but, while larger than $\mathscr{E}_{12}$ and $\mathscr{T}_{11}$, is small in comparison to the combined effects of $\mathscr{P}_{110}$ and $\mathscr{D}_{11}$. The dominant process in the supercritical case is the modification of the gradient production of disturbance energy due to the change in shape of the disturbance, as the plot of $\mathscr{P}_{110}$ demonstrates. However, in contrast to the subcritical case, the rate of energy production is decreased by the nonlinear effects. The value of this term decreases with increasing wavenumber, but the rate of decrease become smaller as the wavenumber increases. Compensating for this, however, the rate of viscous dissipation of the disturbance increases as the wavenumber increases, as the plot of $\mathscr{D}_{11}$ illustrates.

The result is that the Landau constant decreases almost linearly with increasing wavenumber.

4. Conclusions

The calculation of the first Landau constant at the linearly least-stable points for the shear and interactive instabilities has shown that these modes may be either supercritical or subcritical at these wavenumbers. However, even when they are supercritical at the least-stable points, the shear and interactive instabilities are always subcritical at other nearby wavenumbers, and are, therefore, subcritical instabilities. With the thermal-shear mode, however, supercritical behaviour is predicted at all wavenumbers, and this is a supercritical instability.

It has been demonstrated that the weakly nonlinear method is a useful tool in investigating both subcritical and supercritical instability of complex flows. However, the range of validity of the weakly nonlinear calculations must be investigated. In this paper, we have accomplished this by comparison of the lowest-order results with those obtained by including more terms in the perturbation series and by comparison with a direct simulation at a few points. These comparisons show that the predicted threshold amplitudes are accurate only when the magnitude of the amplification rate is small in the subcritical region. However, the direct simulation verifies that the trends predicted by the weakly nonlinear theory are correct for *Re* greater than 6000, even though the predicted threshold amplitudes are not accurate as $|c_i|$ increases. On the other hand, the accuracy of the weakly nonlinear calculations is found to be much better in the supercritical region.

Analysis of the energy sources for the disturbance has shown that subcritical instability occurs at larger wavenumbers primarily because of increased gradient production of disturbance kinetic energy. This is because the shape of the fundamental disturbance changes from that predicted by linear instability theory to a shape more favourable for shear energy production at shorter wavelengths. The results have also demonstrated that many possibly unstable modes may be present at the same values of *Gr*/*Re* and *Re*. All of these modes as well as wave interactions between the modes, must be considered to obtain a comprehensive picture of the instability of mixed convection.

Appendix

The balance of kinetic energy for the fundamental disturbance is given by

$$\begin{aligned}\frac{\partial}{\partial t}\langle\tfrac{1}{2}[\overline{u_1^2}+\overline{v_1^2}+\overline{w_1^2}]\rangle = &-\left\langle\overline{u_1 w_1}\frac{\partial W}{\partial\eta}\right\rangle+\frac{Gr}{Re}\langle\overline{w_1\theta_1}\rangle\\ &-\frac{1}{Re}\left\langle\overline{\left(\frac{\partial u_1}{\partial\eta}\right)^2}+\overline{\left(\frac{1}{\eta+K}\frac{\partial u_1}{\partial\phi}\right)^2}+\overline{\left(\frac{\partial u_1}{\partial z}\right)^2}+\overline{\left(\frac{\partial v_1}{\partial\eta}\right)^2}+\overline{\left(\frac{1}{\eta+K}\frac{\partial v_1}{\partial\phi}\right)^2}\right.\\ &\left.+\overline{\left(\frac{\partial v_1}{\partial z}\right)^2}+\overline{\left(\frac{1}{\eta+K}\frac{\partial v_1}{\partial\phi}\right)^2}+\overline{\left(\frac{\partial w_1}{\partial\eta}\right)^2}+\overline{\left(\frac{\partial w_1}{\partial z}\right)^2}\right\rangle\\ &-\left\langle\overline{u_1^2\frac{\partial u_2}{\partial\eta}}+\overline{\frac{u_1v_1}{\eta+K}\frac{\partial u_2}{\partial\phi}}+\overline{u_1w_1\frac{\partial u_2}{\partial z}}+\overline{u_1v_1\frac{\partial v_2}{\partial\eta}}+\overline{\frac{v_1^2}{\eta+K}\frac{\partial v_2}{\partial\phi}}+\overline{w_1v_1\frac{\partial v_2}{\partial z}}\right.\\ &\left.+\overline{u_1w_1\frac{\partial w_2}{\partial\eta}}+\overline{\frac{w_1v_1}{\eta+K}\frac{\partial w_2}{\partial\phi}}+\overline{w_1^2\frac{\partial w_2}{\partial z}}\right\rangle,\end{aligned} \tag{A 1}$$

where the overbar implies the spatial mean and the brackets $\langle\ \rangle$ imply integration over the volume of the wave. The formulae for the terms in (12) are

$$e_0 = \tfrac{1}{2}\langle \overline{u_{10}^2} + \overline{v_{10}^2} + \overline{w_{10}^2} \rangle, \tag{A 2}$$

$$\mathscr{P}_{101} = -\frac{1}{e_0}\left\langle \overline{u_{10}w_{10}}\frac{\mathrm{d}W_1}{\mathrm{d}\eta} \right\rangle, \tag{A 3}$$

$$\begin{aligned}\mathscr{E}_{12} = -\frac{1}{e_0}\Bigg\langle & \overline{u_{10}^2\frac{\partial u_{20}}{\partial \eta}} + \overline{\frac{u_{10}v_{10}}{\eta+K}\frac{\partial u_{20}}{\partial \phi}} + \overline{u_{10}w_{10}\frac{\partial u_{20}}{\partial z}} + \overline{u_{10}v_{10}\frac{\partial v_{20}}{\partial \eta}} + \overline{\frac{v_{10}^2}{\eta+K}\frac{\partial v_{20}}{\partial \phi}} \\ & + \overline{v_{10}w_{10}\frac{\partial v_{20}}{\partial z}} + \overline{u_{10}v_{10}\frac{\partial w_{20}}{\partial \eta}} + \overline{\frac{w_{10}v_{10}}{\eta+K}\frac{\partial w_{20}}{\partial \phi}} + \overline{w_{10}^2\frac{\partial u_{20}}{\partial z}}\Bigg\rangle,\end{aligned} \tag{A 4}$$

$$\mathscr{P}_{110} = -\frac{1}{e_0}\left\langle (\overline{u_{10}w_{11}} + \overline{u_{11}w_{10}})\frac{\mathrm{d}W_0}{\mathrm{d}\eta} \right\rangle, \tag{A 5}$$

$$\mathscr{T}_{11} = -\frac{Gr}{e_0 Re^2}\langle (\overline{\theta_{10}w_{11}} + \overline{\theta_{11}w_{10}}) \rangle, \tag{A 6}$$

$$\begin{aligned}\mathscr{D}_{11} = -\frac{1}{e_0 Re}\Bigg\langle & \overline{\frac{\partial u_{10}}{\partial \eta}\frac{\partial u_{11}}{\partial \eta}} + \overline{\frac{1}{(\eta+K)}\frac{\partial u_{10}}{\partial \phi}\frac{\partial u_{11}}{\partial \phi}} + \overline{\frac{\partial u_{10}}{\partial z}\frac{\partial u_{11}}{\partial z}} \\ & - \overline{\frac{\partial v_{10}}{\partial \eta}\frac{\partial v_{11}}{\partial \eta}} + \overline{\frac{1}{(\eta+K)}\frac{\partial v_{10}}{\partial \phi}\frac{\partial v_{11}}{\partial \phi}} + \overline{\frac{\partial v_{10}}{\partial z}\frac{\partial v_{11}}{\partial z}} \\ & + \overline{\frac{\partial w_{10}}{\partial \eta}\frac{\partial w_{11}}{\partial \eta}} + \overline{\frac{1}{(\eta+K)}\frac{\partial w_{10}}{\partial \phi}\frac{\partial w_{11}}{\partial \phi}} + \overline{\frac{\partial w_{10}}{\partial z}\frac{\partial w_{11}}{\partial z}}\Bigg\rangle.\end{aligned} \tag{A 7}$$

REFERENCES

Canuto, C., Hussaini, M. Y., Quarteroni, A. & Zang, T. A. 1988 *Spectral Methods in Fluid Dynamics*. Springer.

Davey, A. & Nguyen, H. P. F. 1971 Finite-amplitude stability of pipe flow. *J. Fluid Mech.* **45**, 701–720.

Fujimura, K. 1989 The equivalence between two perturbation methods in weakly nonlinear stability theory for parallel shear flows. *Proc. R. Soc. Lond.* A **424**, 373–392.

Kemeny, G. A. & Somers, E. V. 1962 Combined free and forced convection in vertical circular tubes – Experiments with water and oil. *Trans. ASME* C: *J. Heat Transfer* **108**, 392–397.

Kleiser, L. & Schumann, U. 1980 Treatment of incompressibility and boundary conditions in three-dimensional numerical spectral simulations of plane channel flows. In *Proc. 3rd GAMM Conference on Numerical Methods in Fluid Mechanics* (ed. E. H. Hirschel), pp. 165–173. Vieweg.

Kleiser, L. & Schumann, U. 1984 Spectral simulations of the laminar-turbulent transition process in plane Poiseuille flow. In *Spectral Methods for Partial Differential Equations* (ed. R. G. Voight, D. Gottlieb & M. Y. Hussaini), pp. 141–163. SIAM.

Maitra, D. & Subba Raju, K. 1975 Combined free and forced convection laminar heat transfer in a vertical annulus. *Trans. ASME* C: *J. Heat Transfer* **97**, 135–137.

Marcus, P. S. 1981 Effects of truncation in modal representations of thermal convection. *J. Fluid Mech.* **103**, 241.

Orszag, S. A. 1972 Numerical simulation of incompressible flows within simple boundaries I. Galerkin (spectral) representation. *Stud. Appl. Maths* **50**, 293–327.

Rogers, B. B. & Yao, L. S. 1993*a* The effects of Prandtl number on mixed-convection instability in a vertical annulus. *Trans. ASME* C: *J. Heat Transfer* (to appear).

Rogers, B. B. & Yao, L. S. 1993*b* Natural convection in a heated annulus. *Intl J. Heat/Mass Transfer* **36**, 35–47.

SCHEELE, G. F. & HANRATTY, T. J. 1962 Effect of natural convection on stability of flow in a vertical pipe. *J. Fluid Mech.* **14**, 244–256.

SEN, P. K. & VENKATESWARLU, D. 1983 On the stability of plane Poiseuille flow to finite-amplitude disturbances, considering the higher-order Landau coefficients. *J. Fluid Mech.* **133**, 179–206.

STUART, J. T. 1958 On the non-linear mechanics of hydrodynamic instability. *J. Fluid Mech.* **4**, 1–21.

STUART, J. T. 1960 On the non-linear mechanics of wave disturbances in stable and unstable parallel flows. Part 1. The basic behaviour in plane-Poiseuille flow. *J. Fluid Mech.* **9**, 353–370.

YAO, L. S. & ROGERS, B. B. 1989*a* The linear stability of mixed convection in a vertical annulus. *J. Fluid Mech.* **201**, 279–298.

YAO, L. S. & ROGERS, B. B. 1989*b* Mixed convection in an annulus of large aspect ratio. *Trans. ASME* C: *J. Heat Transfer* **111**, 683–689.

YAO, L. S. & ROGERS, B. B. 1992 Finite-amplitude instability of nonisothermal flow in a vertical annulus. *Proc. R. Soc. Lond.* A **437**, 267–290 (referred to herein as YR).